

Kilohertz QPOs in low-mass X-ray binaries as oscillation modes of tori around neutron stars: I.

Marcio G B de Avellar^{1,2,*}, Oliver Porth², Ziri Younsi², Luciano Rezzolla^{2,3}

¹*Instituto de Astronomia, Geofísica e Ciências Atmosféricas, Universidade de São Paulo, 05508-090, São Paulo, Brasil*

²*Institut für Theoretische Physik, Johann Wolfgang Goethe-Universität, Max-von-Laue-Str. 1 60438, Frankfurt am Main, Germany*

³*Frankfurt Institute for Advanced Studies, Ruth-Moufang-Strasse 1, 60438 Frankfurt am Main, Germany*

1 March 2022

ABSTRACT

There have been many efforts to explain the dynamical mechanisms behind the phenomenology of quasi-periodic oscillations (QPOs) seen in the X-ray light curves of low-mass X-ray binaries. Up to now, none of the models can successfully explain all the frequencies observed in the power spectral density of the light curves. After performing several general-relativistic hydrodynamic simulations of non-selfgravitating axisymmetric thick tori with constant specific angular momentum oscillating around a neutron star such as the one associated with the low-mass X-ray binary 4U 1636-53, we find that the oscillation modes give rise to QPOs similar to those seen in the observational data. In particular, when matching pairs of kilohertz QPOs from the numerical simulations with those observed, certain combinations reproduce well the observations, provided we take a mass for the neutron star that is smaller than what generally assumed. At the same time, we find that tori with constant specific angular momentum cannot match the entire range of frequencies observed for 4U 1636-53 due to physical constraints set on their size. Finally, we show that our results are consistent with the observed shifts in QPO frequency that could accompany state transitions of the accretion disc.

Key words: accretion, accretion discs – relativity – stars: oscillations – X-rays: binaries.

1 INTRODUCTION

Several X-ray variability components can be seen in the power spectral density (PSD) of the X-ray light curves of neutron-star and black-hole low-mass X-ray binaries (NS- and BH-LMXBs, respectively). Among other components, there is a vast set of quasi-periodic oscillations (QPOs) ranging from ~ 0.01 to ~ 1000 Hz, whose physical origin (origins) is still an open problem (see [van der Klis 2006](#), for a comprehensive review of QPOs in LMXBs). Overall, there are two broad classes of models that address the mechanism behind the QPOs with different degrees of success. The first one relies on orbital motions (including the general-relativistic epicyclic motions) of matter around the compact object and their timescales (see, for example, [Miller et al. 1998](#); [Stella & Vietri 1999](#); [Abramowicz et al. 2004](#)). The second class, the focus of this study, interprets the QPOs as oscillations and/or flow instabilities of some kind of an accretion disc orbiting around the central object (see, for example, [Rezzolla et al. 2003b](#)). The study of accretion flows around compact objects dates back to the 1970s with the pioneering works of [Shakura & Sunyaev \(1973\)](#) and [Novikov & Thorne \(1973\)](#) when considering geometrically thin accretion discs, and to the works of [Fishbone & Moncrief \(1976\)](#); [Abramowicz et al. \(1978\)](#); [Kozłowski et al. \(1978\)](#) in the opposite case of

geometrically thick discs. The latter are possible solutions of a stationary and axisymmetric fluid that undergoes a non-Keplerian circular motion around a compact object. Despite the variety of mechanisms proposed so far, the scarcity of the observational data and the weak constraints it poses, do not seem to favour one model over the other.

Astronomical observations over the years have revealed that the frequencies of different QPOs observed in a given source correlate with each other through very specific patterns and, more importantly, that the same patterns are then seen across systems of the same type (e.g., [van Straaten et al. 2002, 2003](#); [Reig et al. 2004](#); [van Straaten et al. 2005](#); [Altamirano et al. 2008](#)). The correlations seen in the PSDs of different types of X-ray binaries, i.e., containing black holes, neutron stars or white dwarfs, seem to indicate that a common component of these systems, most likely the accretion disc, is responsible for the origin of these variability features (e.g., [Wijnands & van der Klis 1999](#); [Psaltis et al. 1999](#); [Mauche 2002](#); [Warner & Woudt 2002](#)). Within this accretion-disc interpretation, the highest frequency QPOs, known as the lower (ν_l) and upper (ν_u) kilohertz QPOs (kHz QPOs), are thought to reflect the properties of the accretion flow in the vicinity of black holes and neutron stars, where effects of the general relativity are expected (see [van der Klis 2006](#)).

Other properties of the QPOs, besides the frequency itself, like the fractional amplitude, quality factor, and time/phase lags,

* E-mail: mgb.avellar@iag.usp.br

also depend on the spectral state of the source, which can be parametrized by the position of the source in what is called the “colour-colour diagram” (CCD) in X-rays (e.g., [Hasinger & van der Klis 1989](#); [Wijnands et al. 1997](#); [van Straaten et al. 2002](#); [Di Salvo et al. 2003](#); [Méndez 2006](#); [Altamirano et al. 2008](#); [de Avellar et al. 2016](#)). The changes in the the position of the source within the CCD are therefore expected to reflect, at least qualitatively, different configurations of the flow near the central compact object (see [Altamirano et al. 2008](#), for example).

From the theoretical point of view, geometrically thick discs achieved astrophysical relevance once it was demonstrated that external perturbations cause them to oscillate periodically, opening new avenues for the interpretation of the phenomenology of QPOs (e.g., [Zanotti et al. 2003](#); [Rezzolla et al. 2003b](#); [Lee et al. 2004](#); [Abramowicz et al. 2004](#); [Zanotti et al. 2005](#); [Blaes et al. 2006](#); [Remillard & McClintock 2006](#); [Rezzolla et al. 2003b](#); [Abramowicz et al. 2003](#); [Bursa et al. 2004](#); [Kluźniak et al. 2004](#); [Schnittman & Rezzolla 2006](#); [Blaes et al. 2007](#); [Montero & Zanotti 2012](#); [Mazur et al. 2013](#); [Vincent et al. 2014](#); [Bakala et al. 2015](#); [Mishra et al. 2017](#), and references therein for the vast literature that has developed over the years). In particular, [Rezzolla et al. \(2003a\)](#) identified the frequencies in the X-ray spectra of BH-LMXBs as inertial-acoustic modes, or p -modes, of a relativistic geometrically-thick toroidal accretion disc. The model is successful in reproducing approximately the 3:2 ratio seen in the range of the high-frequency (HF) QPOs observed in these kinds of systems. Further investigations of the properties of axisymmetric p -mode oscillations were later on performed by, for example, [Zanotti et al. \(2003, 2005\)](#); [Montero et al. \(2007, 2008, 2010\)](#), through general-relativistic hydrodynamical (GRHD) simulations of both non-selfgravitating and selfgravitating tori around compact objects.

This paper extends these simulations to NS-LMXBs, with particular application to the Atoll¹ source 4U 1636–53, for which more than 15 years of X-ray data have been collected and analysed in their many aspects (see, for example, [Di Salvo et al. 2003](#); [Casares et al. 2006](#); [Barret et al. 2006](#); [Altamirano et al. 2008](#); [Lin et al. 2011](#); [Sanna et al. 2012](#); [Artigue et al. 2013](#); [de Avellar et al. 2013](#); [Sanna et al. 2014](#); [Lyu et al. 2014](#); [de Avellar et al. 2016](#); [Zhang et al. 2017](#); [Ludlam et al. 2017](#), for an incomplete set of references; see references therein). More specifically, this paper details how we build a sequence of 21 relativistic and axisymmetric tori with constant specific angular momentum and follow their oscillations triggered by a small radial and vertical velocity perturbation.

The plan of the paper is as follows. In Sec. 2.3, we discuss how frequencies are identified from the simulation data and cross-compared to the observational ν_l - ν_u relation (Section 3). The results are discussed in Sec. 4 elucidating the implications of our analysis with application to the changing properties of the kHz QPOs as the source moves across the CCD. Throughout we adopt the geometrized system of units $G = c = 1$, with G Newton’s constant and c the speed of light.

2 NUMERICAL SETUP

2.1 Initial configurations of the tori

As a first step we describe the construction of the initial equilibrium torus solutions of which the oscillation frequencies are anal-

ysed in the remainder of this paper. We consider tori as stationary non-selfgravitating fluid configurations that can be built around a compact object as a solution for the GRHD equations (as in [Kozłowski et al. 1978](#), for example). To simulate the dynamics of this system we solve the usual GRHD equations written in their covariant form

$$\nabla_\mu (\rho u^\mu) = 0, \quad (1)$$

$$\nabla_\mu T^{\mu\nu} = 0, \quad (2)$$

where ρ is the rest-mass density, u^μ are the (contravariant) components of the fluid four-velocity and $T^{\mu\nu}$ is the energy-momentum tensor (see, for example, [Rezzolla & Zanotti 2013](#)).

To close the system of equations (1) and (2) we assume an ideal-fluid equation of state ([Rezzolla & Zanotti 2013](#)) $p = \rho\epsilon(\hat{\gamma} - 1)$, where ϵ is the specific internal energy and $\hat{\gamma}$ is the adiabatic index. The initial (test-fluid) equilibrium is obtained as isentropic configuration, thus we set the entropy $\kappa = p/\rho^{\hat{\gamma}}$ to an arbitrary constant (we have taken $\kappa = 0.001$)². As a result, the specific enthalpy $h(\rho, p)$ is expressed as

$$h = 1 + \epsilon + \frac{p}{\rho} = 1 + \frac{\hat{\gamma}}{\hat{\gamma} - 1} \frac{p}{\rho}. \quad (3)$$

Since the fluid is following a non-Keplerian motion, the distribution of specific angular momentum $\ell := u_\phi/u_t$ needs to be specified, where u_ϕ, u_t are the azimuthal and time components of the four-velocity, respectively. The simplest choice in this case, and the one that has been historically best studied, is to set $\ell = \text{const.}$, so that the maximum equatorial torus size for the marginally stable non-accreting configuration is determined by the value of the specific angular momentum distribution for the fluid ([Font & Daigne 2002](#); [Daigne & Font 2004](#); [Rezzolla & Zanotti 2013](#)).

As mentioned in Sec. 1, we use the NS-LMXB in 4U 1636–53 as our study case, and the torus should therefore not penetrate the surface of the star, assumed to have a mass which falls in the uncertainty bracket suggested by [Casares et al. \(2006\)](#), i.e., $M = 1.7 M_\odot$. Assuming the representative nuclear-physics equation of state SLy4 of ([Douchin & Haensel 2001](#)), to such a mass would correspond to a neutron star with radius of 11.42 km when nonrotating.

Since the exterior spacetime is given by the Schwarzschild solution with M the mass of the neutron star, we choose values of the constant specific angular momentum $\ell \in [3.68, 3.81]$, noting that a torus with $\ell = 3\sqrt{6}/2 \simeq 3.67$ is actually a ring ([Rezzolla & Zanotti 2013](#)). We recall, in fact, that the position of the cusp and the centre, which are the location where the specific angular momentum coincides with the corresponding Keplerian one, are both at $6M$ for a nonrotating central star of mass M and the orbital frequency of the fluid in this case tends to the orbital frequency of a test particle. Hence, a torus with $\ell \geq 3.81$ would penetrate the stellar surface, i.e., it would have $r_{\text{cusp}} < r_{\text{star}}$.

Also, in order to minimise mass loss at each oscillation, we employ a jump in the effective potential, $\Delta W := W_{\text{in}} - W_{\text{cusp}}$, where W_{in} is the potential at the inner edge of the torus and W_{cusp} is the potential at the cusp of the of the potential well, specifying W_{in} in a way that the size of the torus is $\simeq 90\%$ of the maximum equatorial torus size for the marginally stable non-accreting configuration. Hence, the inner edge of each torus is always safely below

¹ For a description of the Z and Atoll sources, see [Hasinger & van der Klis \(1989\)](#)

² We recall that ideal-fluid and the polytropic equations of state coincide for isentropic transformations as it is the case for the initial data [Rezzolla & Zanotti \(2013\)](#).

Table 1. Parameters of the models built and simulated in this work. Reported are: the resolution, specific angular momentum (ℓ_o), the position of the cusp (r_{cusp}), the position of the inner edge of the torus (r_{in}), the position of the centre of the torus (r_{centre}), the outer edge of the torus (r_{out}) and the size of the torus (* *); for each quantity the corresponding units are indicated in the square. Note that only the odd-numbered models from Tor.03 to Tor.21 have been simulated numerically.

Models	resolution	$\ell_o [M^2]$	$r_{\text{cusp}} [M]$	$r_{\text{in}} [M]$	$r_{\text{centre}} [M]$	$r_{\text{out}} [M]$	size [km] (* *)
Tor.03	$2624 \times 1728 *$	3.6932	5.3607	5.5617	6.7774	7.8297	5.69
Tor.05	$1920 \times 1280 *$	3.7064	5.1908	5.4529	7.0437	8.6271	7.97
Tor.07	$1472 \times 960 *$	3.7196	5.0606	5.3693	7.2707	9.4006	10.12
Tor.09	$1216 \times 832 *$	3.7328	4.9533	5.2951	7.4753	10.1923	12.29
Tor.11	1040×700	3.7460	4.8612	5.2306	7.6649	11.0196	14.53
Tor.13	900×600	3.7592	4.7801	5.1721	7.8439	11.9001	16.89
Tor.15	780×520	3.7724	4.7075	5.1170	8.0148	12.8531	19.42
Tor.17	680×460	3.7856	4.6416	5.0575	8.1793	13.9106	22.22
Tor.19	600×400	3.7988	4.5812	5.0073	8.3386	15.0653	25.25
Tor.21	560×380	3.8062	4.5494	4.9771	8.4262	15.7797	27.12

(*) resolution reached in the torus area after three levels of mesh refinement.

(* *) assuming a neutron star mass of $1.7 M_{\odot}$.

the inner edge of the marginally stable one. Following the prescription described above and which resembles what suggested by Font & Daigne (2002), we have built 21 axisymmetric torus models of increasing size; the main properties of some of these models are summarised in Table 1.

The oscillations are triggered by specifying small radial and vertical perturbations in the 4-velocity field given by

$$(\delta v^i) = \left(0, \frac{\eta}{\sqrt{2} g_{rr}}, \frac{\eta}{\sqrt{2} g_{\theta\theta}}, 0 \right), \quad (4)$$

where $\eta := 0.01 \sqrt{W_{\text{in}} - W_{\text{centre}}}$ and W_{centre} is the potential at the centre of the torus and which also corresponds with the position of the maximum rest-mass density, ensuring that the perturbation in the vertical and radial directions have the same magnitude as can be readily seen by computing the scalar product $\delta v^i \delta v_i = \eta^2$. Since the quantity $\sqrt{W_{\text{in}} - W_{\text{centre}}}$ is proportional to the “escape velocity” from the potential well, the perturbation in the velocity is comparable across all torus models.

2.2 Numerical approach

The simulations were carried out using the black-hole accretion code BHAC (Porth et al. 2017), which solves the ideal general-relativistic magnetohydrodynamic (GRMHD) equations in arbitrary spacetimes, exploiting shock-capturing techniques and adaptive mesh refinement. For a detailed description of the code and its capabilities see Porth et al. (2017). BHAC is a versatile code that allows the user to freely choose the metric theory of gravity and coordinate system. Here we use the Schwarzschild metric in modified Kerr-Schild coordinates, whose main purpose is to remove the coordinate singularity at the horizon but also to stretch the grid radially thus reducing the computational cost.

Our grid extends from the neutron star radius at $r_{\text{star}} \simeq 4.549 M$ to $30 M$ in the radial direction and from $\pi/2 - 0.628$ to $\pi/2 + 0.628$ in the θ direction. The resolution of the grid was chosen in order to resolve all tori with $\simeq 200$ cells in their diameter. Since uniform resolution would have been impractical for simulations of small tori, three levels of mesh refinement were employed in the the smallest tori (cf. Table 1).

2.3 Adopted methodology for the data analysis

Although we have constructed 21 models different initial models representing stationary tori, our evolutions have been performed using only the odd-numbered models from Tor.03 to Tor.21, for a total of ten models simulated. This choice was dictated by the need to reduce the computational costs but does not come at the cost of reducing the generality of our results and conclusions. Also, models smaller than Tor.03 were not considered because they turn out too small to be physically meaningful. We recall, in fact, that as the torus’ size goes to zero (both in the radial and in the polar directions), the corresponding oscillations approach those of a test particle at the position of the centre, which can be readily computed analytically Rezzolla et al. (2003b); Zanotti et al. (2003).

We have therefore evolved each of the ten models up to $t = 60\,000 M$, which is equivalent to $\simeq 500$ orbital periods, and corresponds to a timescale of ~ 500 ms when assuming $M = 1.7 M_{\odot}$. Due to the velocity perturbation, the tori will oscillate inside the potential well, possibly leading to mass loss or induced accretion at each period. Specifying W_{in} as mentioned in Sec. 2.1 and as shown in Table 1 we minimise this effect. As a result, the oscillation can survive in all runs with only a minimal damping due to the mass loss; no significant drift in frequencies is observed as a consequence of this prescription.

Rezzolla et al. (2003b) and Zanotti et al. (2003) studied toroidal fluid configurations around Schwarzschild black holes having a constant specific angular momentum distribution; the analysis by Rezzolla et al. (2003b) was semi-analytical and involved linear perturbation theory, while the analysis by Zanotti et al. (2003) was fully numerical and involved general-relativistic hydrodynamic simulations. Notwithstanding the two different approaches, both analyses found that the p -modes of these configurations appear in frequencies obeying the $2 : 3 : 4 : \dots$ ratio. Zanotti et al. (2005), on the other hand, studied through both linear analysis and simulations, toroidal fluid configurations around Kerr black holes also having non-constant specific angular-momentum distributions; as a result, a richer set of frequencies was simulated and measured. The linear perturbative analysis formulated a prediction about the eigenfrequencies of the p -modes and the ratio in which they appear, thus providing a theoretical insight into where

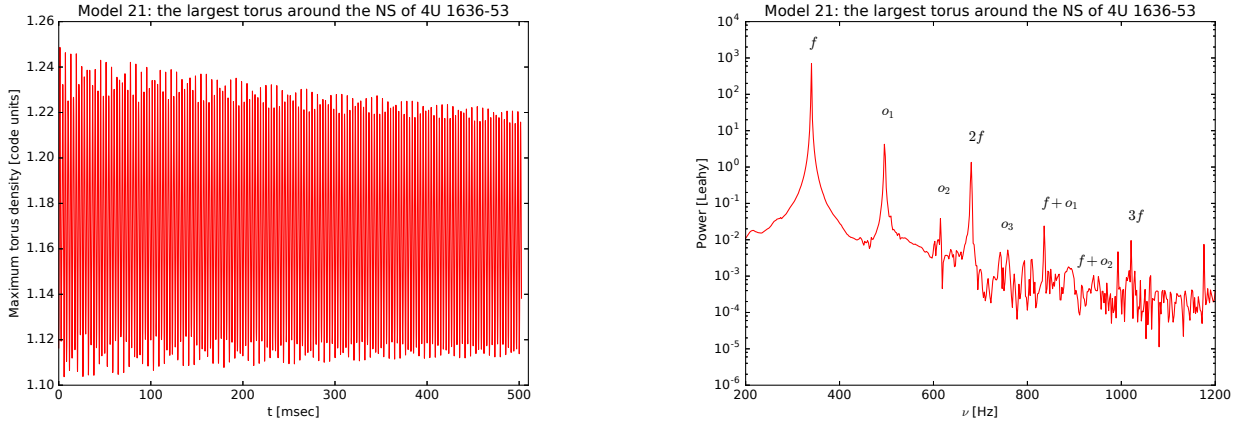


Figure 1. Oscillations in the the maximum rest-mass density (left panel) and its corresponding PSD (right panel) of Tor. 21 , the largest torus around the neutron star in 4U 1636–53 (see Table 1). The small damping in the density is due to $\sim 1\%$ mass loss, which is also the largest measured in our simulations. Other tori show very similar behaviours, with the position and amplitude of the modes obviously depending on the specific torus considered.

to look for the frequencies coming from the simulations. In either case, the authors studied the response of the L_2 -norm of the density which as a global quantity is particularly suitable for comparisons with the results coming from the perturbative analysis.

In our analysis we have followed the periodic response of the central rest-mass density of the tori (ρ_{max}) to the velocity perturbation. The choice for the central density is physically motivated in the sense that it is where the concentration of matter is larger and where most likely the variations in (X-ray) luminosity occur, i.e., where the QPOs would come from (see Schnittman & Rezzolla 2006; Vincent et al. 2014).

We note that the responses of a given hydrodynamical quantity, e.g., the central rest-mass density and of its L_2 -norm over the computational domain Ω , i.e., $L_2(\rho) := \sqrt{\int_{\Omega} \rho^2 dV / \int_{\Omega} dV}$, should be equivalent. However, it was found that while the frequency of the peaks remains the same for both quantities, the strength of the peaks and even their appearance depend to varying degree on the quantity under consideration. This fact raises the question of how to appropriately identify the peaks to be considered in the analysis and as a consequence a suitable strategy was developed for this purpose (see discussion in Sec. 2.3.1 below). Figure 1 reports the oscillations of the central rest-mass density ρ_{max} and its corresponding PSD for Tor. 21 , which the largest torus around the neutron star in 4U 1636–53. The mass lost in this case is the largest of all the models considered, but it is only of the order of 1%.

2.3.1 Frequency identification

In order to proceed with the identification of the modes observed, we have followed the linear analysis by Rezzolla et al. (2003b); Zanotti et al. (2003) and Zanotti et al. (2005), and first identified and labelled the p -mode fundamental frequency and its overtones using the same nomenclature, as shown in the right panel of Fig. 1 for the representative torus model Tor. 21 . Proceeding in this manner, we were able to determine eight different frequencies of increasing value: f , o_1 , o_2 , $2f$, o_3 , $f + o_1$, $f + o_2$, and $3f$. These peaks in the PSD correspond to the same frequencies identified by Zanotti et al. (2005) in their analysis, with the potential addition

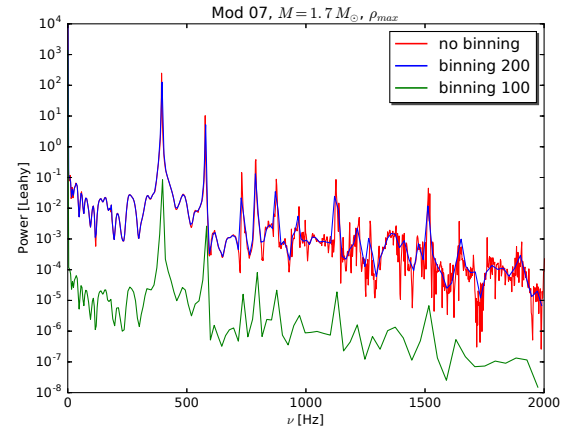


Figure 2. Examples of binned and not binned PSDs of the maximum rest-mass density. The data refers to the model Tor. 21 and shows that even a low binning rate retains the main features of the PSDs.

of the third overtone labelled o_3 , whose excess power is however rather small.

However, we recall that not all frequencies are detected in all models. Additional tests were performed to ensure that in this study of the QPOs only reliable peaks were used. More information can be gained by logarithmically binning our data and comparing the binned PSDs with the non-binned ones³. Logarithmically rebinning the data and averaging the same number of points per decade results in a rebinning factor of $10^{1/N}$. Performing the binning correctly will add power to a feature which is present in the data while smearing out the noise. Hence, we have adopted two binning factors to determine whether a given peak was genuine of the possible contamination from noise: $N = 200$ (infrequent binning) and $N = 100$ (frequent binning). An example of this procedure is illustrated in Fig. 2 for Tor. 07 .

In this way, a systematic study of the statistics of the vari-

³ Rebinning by a factor N means that N points are taken and averaged into a single value

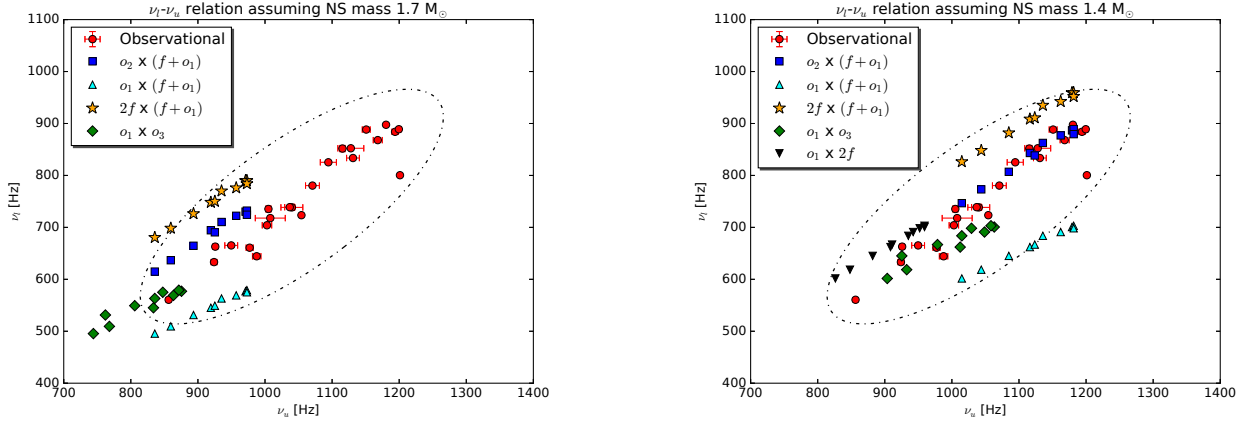


Figure 3. Selected pairs of peaks in the PSD whose numerical relations are presented in Table 2. A larger torus gives rise to lower characteristic frequencies, while higher masses for the central star result in lower frequencies. The lower the value of the neutron star mass, the higher the values of the frequencies of the peaks. The frequencies of the simulated peaks are scalable with the mass of the neutron star, $\nu_1/\nu_2 = M_2/M_1$, as are the peak separations $\Delta\nu_1/\Delta\nu_2 = M_2/M_1$. The dot-dashed ellipse delineates a region around the observational relation where suitable choices of pairs of peaks are found.

Table 2. Ratio between the frequencies of the selected modes measured from the simulations. Each values reports the ratio between the frequency of the mode shown horizontally with the frequency of the mode shown vertically. Shown in boldface in the bottom right corner of the Table is the ratio of the frequencies of the upper and lower kHz QPOs, ν_u/ν_l , for the source NS-LMXB 4U 1636–53.

		ν_u : higher kHz QPO					
		f	o_1	o_2	$2f$	o_3	$f + o_1$
ν_l : lower kHz QPO	f		1.46	1.81–1.86	2.00	2.10–2.23	2.46
	o_1			1.24–1.27	1.36	1.43–1.52	1.68
	o_2				1.08	1.15–1.21	1.32–1.36
	$2f$					1.05–1.11	1.23
	o_3						1.11–1.17
	ν_l						1.30–1.53

ous models was performed through which we counted how often a given peak was detected “robustly” through all simulation models. By “robust”, we here refer to a peak that needed to be detected for at least seven torus models and both in the PSD of the maximum rest-mass density and in the PSD of the corresponding L_2 -norm. This validation was necessary to obtain the confidence that the peak considered actually referred to a physical mode of oscillation. Following these criteria for the identification of the peaks in the PSD and for the determination of their robustness, the following frequencies were ultimately selected: f , o_1 , o_2 , $2f$, o_3 and $f + o_1$. The peaks associated with the frequencies $f + o_2$ and $3f$ did not pass these tests and were therefore not considered in the subsequent analysis, even though they appear clearly in some models.

3 RESULTS AND DISCUSSION

A first and possibly most important result of our analysis is that the most prominent peaks of the oscillation modes of tori around neutron stars obey specific ratios, as shown in Table 2, and in agreement with the linear analysis performed by Rezzolla et al. (2003a) and by Zanotti et al. (2003). A summarising representation of this conclusion is presented in Fig. 3, where we show the observational $\nu_l \times \nu_u$ relation for the NS-LMXB 4U 1636–53, together with some

choices of pairs of peaks (the frequencies of the modes of oscillation) produced by the simulated oscillating tori. In the following discussion we will concentrate on two specific cases, as these are the most representative and interesting.

The chosen frequency pairs reported in Fig. 3 are meant to match the lower (ν_l) and the upper (ν_u) kHz QPOs. Red dots represent the observed data while the points with colours different from red represent the frequencies measured from our simulated tori. Clearly, all of the simulated data sets shows a remarkably linear relation between the chosen frequencies. In addition, we have also found that there is a nonlinear relation between the torus size and oscillation frequency with an overall deviation of $\sim 10\%$ over all considered models. As shown in Fig. 4, larger tori display in general smaller frequencies. However, below a critical torus size of $\simeq 12\text{km}$ (for a stellar mass of $1.4M_\odot$) all frequencies start to decrease as the size of the torus is decreased.

Since the oscillation frequencies are related to the typical timescales associated with the central object, and thanks to the simplicity of the Schwarzschild metric which we use for the exterior of the relativistic star, the only degree of freedom is the stellar mass M . As a result, all of the reported frequencies can be scaled simply as $\nu_1/\nu_2 = M_2/M_1$. Stated differently, decreasing the mass of the neutron star shifts the peaks to higher frequencies. However, although the mass of the compact object does not change the ratio between the peaks, i.e., ν_u/ν_l , it affects the peak separation between these two peaks in the same ratio M_2/M_1 . This is behaviour is clearly shown by the dual representation in the two panels of Fig. 3, where the left panel shows the effect of assuming a neutron-star mass of $M = 1.7 M_\odot$. The right panel, on the other hand, reports the same data and the corresponding correlations when the mass of the star is assumed to be $M = 1.4M_\odot$. In this case, one can see that three choices of pairs of peaks provide all rather good representations of observational relation: peaks o_1 and $2f$ (black upside down triangles), peaks o_1 and o_3 (green diamonds) and peaks o_2 and $f + o_1$ (blue squares). At the same time, we should recall that this value of the mass for the neutron star is smaller of what estimated by Casares et al. (2006), who have constrained the mass of the central compact object in 4U 1636–53 to be in the range $1.6M_\odot < M < 1.9M_\odot$.

In addition, as can be seen in the two panels of Fig. 3, not

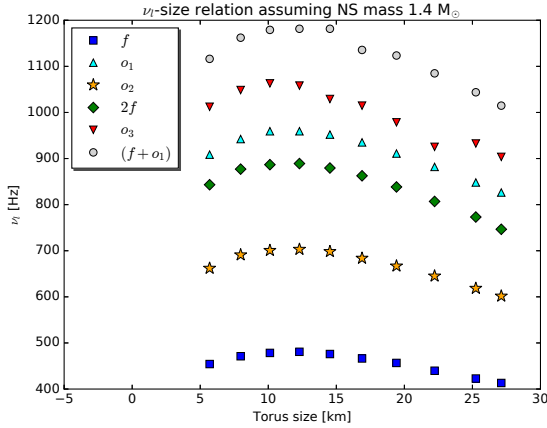


Figure 4. Frequency-size relation for a neutron star of mass $M = 1.4 M_{\odot}$ and where different colours refer to different oscillation modes. Note that there is a general nonlinear behaviour yielding larger frequencies for smaller tori.

all choices of pairs of peaks can match the observed linear relation between the observed frequencies. In fact, assuming the mass of the neutron star to be in the range given by [Casares et al. \(2006\)](#), i.e., $M = 1.7 M_{\odot}$, no choice can match the observational relation except the pair of peaks o_1 and o_3 (green diamonds) and o_2 and $f + o_1$ (blue squares), but only when the neutron star is assumed to have a mass $M = 1.4 M_{\odot}$; even in these cases, however, the match is marginal. More specifically, in the case of peaks o_1 and o_3 , although the slope of the correlation and the peak separation seem to be in agreement with the observational relation, the smallest physically meaningful torus, which displays the highest frequencies in this sequence, only reaches the lowest frequencies of the observational relation (see left panel of Fig. 3). Similarly, the modes o_2 and $f + o_1$, although promising since they match the observed relation for high frequencies, i.e., for $[\nu_{o_2}, \nu_{f+o_1}] > [740, 1010]$ Hz, do not extend to the low-frequency end of the observational relation.

Before concluding this section a few considerations are worth making. First, since the constant- ℓ torus size is delimited from above by the requirement that it does not penetrate the neutron star surface (thus delimiting the frequencies from below), and the oscillation frequencies achieve their maximum at finite torus extent, the range of achievable frequencies is fixed by the model.

Second, we recall that we have here used the SLy4 equation of state, for which a nonrotating star with mass $M = 1.7 M_{\odot}$ has a radius of 11.42 km. On the other hand, if the star is assumed to have a mass $M = 1.4 M_{\odot}$ the radius is 11.67 km, thus extending the range of sizes of the possible tori. Hence the equation of state chosen for the neutron star does play a role in the sense that it defines, through the radius of the star, the boundary of our simulations as well as the maximum size of the torus. Indeed, regarding the $1.4 M_{\odot}$ case, it would require building a torus bigger than the ones considered so far. Opposite considerations apply for the mode peaks o_1 and $2f$ (black inverted triangles) and o_1 and o_3 (green diamonds). Both pairs match the low-frequency tail of the observed linear correlation when $M = 1.4 M_{\odot}$, but not the high-frequency end. Going to smaller neutron-star masses would not help much in this case, since to increase the frequencies one would need to reduce the torus' size by reducing the value of the specific angular momentum, which is however very close to the minimum attainable i.e., $\ell \simeq 3.67$ ([Rezzolla & Zanotti 2013](#)); in fact, as remarked

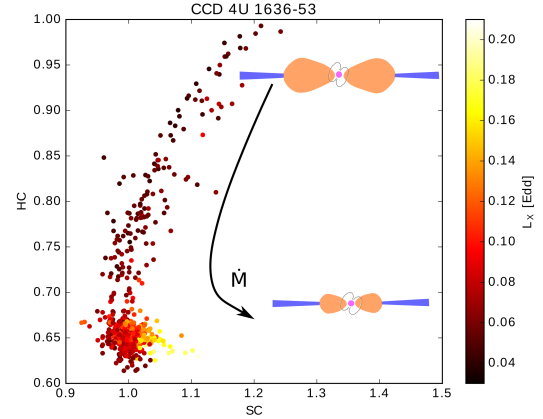


Figure 5. Colour-colour diagram (CCD), where the horizontal and vertical axes represent the “hard colour”, HC and the “soft colour”, SC, respectively. (see main text for details) Larger tori show lower frequencies in general and should be placed in the upper parts of the CCD, where the frequencies are, in general, lower, especially for the upper kHz QPO. Also shown schematically is the direction of increase of the mass-accretion rate and a cartoon showing two suggested states of the accretion disc: in the upper part the mass-accretion rate is low and the disc is farther away from the central object, allowing a bigger torus and lower QPOs. Conversely, in the lower part, the accretion rate is high and the disc is closer to the central object, compressing the torus and yielding higher QPOs. This framework can be used to explain both the observations and the results of the simulations (see main text for details).

above, models smaller than $\text{TOR} . 03$ would be difficult to justify physically because of their small size (cf. Table 1).

Third, although the oscillation modes found do not match exactly the entire observed kHz QPOs frequency relation, this approximation provides more information than was previously expected. We recall that the observed $\nu_l - \nu_u$ relation, which is detectable when both the lower and the upper kHz QPOs appear, is thought to arise from the rapidly changing environment around the neutron star. Indeed, the appearance of both kHz QPOs occurs only in the left lower corner of the CCD, which is also the region of the CCD where the system changes considerably ([Zhang et al. 2017](#)). We show in Fig. 5 the CCD for 4U 1636–36, together with the corresponding X-ray luminosity as indicated by the colorcode in units of the Eddington luminosity. Recalling that the CCD depends on the definition the hard and soft colours and following [Altamirano et al. \(2008\)](#), we define the “hard colour” (HC) as the $9.7 - 16.0$ keV/ $6.0 - 9.7$ keV count-rate ratio and the “soft colour” (SC) as the $3.5 - 6.0$ keV/ $2.0 - 3.5$ keV count-rate ratio, respectively. Note that the X-ray luminosity is higher in the region of the CCD where both kHz QPOs are simultaneously detected, thus enabling the detection $\nu_l - \nu_u$ observational relation [see [Zhang et al. \(2017\)](#) and references therein for more details]. Since the p -mode frequencies of the tori are in first approximation related to their size, the sequence of tori considered here could represent different states of 4U 1636–53. More specifically, it is plausible to imagine that an external mechanism, possibly within the accretion flow, could determine the size of the torus at a given moment as the source moves across the CCD, perturbing the torus in the process.

Since there is an anticorrelation between the frequencies of the QPOs and the hard colour for Atoll sources ([Linares 2009](#)),

specially for the upper kHz QPOs⁴, it is then tempting to place the tori in the CCD according to their sizes and we envisage that larger tori are placed in the upper right corner of the CCD (when the source is in the hard state) and smaller tori are placed in the lower left corner of the CCD (when the source is in the soft state) as depicted schematically in Fig. 5. We conjecture, therefore, that the variation of the X-ray luminosity across the CCD is responsible, through the accretion rate, for changes in size of the torus around the neutron star. This idea is reported schematically using the data of 4U 1636–53 also in Fig. 5: as the accretion rate increases from hard to soft states (see, for example, Liu et al. 2005; Done et al. 2007, and references therein), so does the X-ray luminosity and the accretion disc extends closer to the surface of the neutron star. Consequently, the overall observational picture seems to be consistent with placing large tori in hard states – when the disc is expected to be more distant and the tori can “expand” – and small tori in soft states – when the disc is “compressed” as a result of the increased accretion rate.

Finally, we can compare and contrast our results with those obtained recently by other groups. In particular, we note that our results are in agreement with those of Török et al. (2016), where the authors employ a similar idea, but consider non-axisymmetric frequencies. Their work is based on the analysis by Straub & Šrámková (2009), who derived pressure-corrected fully general-relativistic expressions for the eigenfunctions and eigenfrequencies of the radial and vertical epicyclic modes of a slightly non-slender, constant specific angular momentum torus. Török et al. (2016) built a sequence of tori with different thicknesses and for each model they found the modes of oscillation, identifying the lower and upper kHz QPOs with the frequency of the non-axisymmetric $m = -1$ radial epicyclic mode and the Keplerian frequency at the centre of the torus, respectively. In this way they were able to match the $\nu_l - \nu_u$ relation for the kHz QPOs considerably better than previous models, such as the relativistic-precession model (Stella & Vietri 1999), constraining the mass of the neutron star in 4U 1636–53 to be $M = 1.69 M_\odot$. More recently, Parthasarathy et al. (2017) performed axisymmetric ideal-MHD Newtonian simulations of oscillating cusp-filling tori orbiting a nonrotating neutron star. They followed the response of the mass-accretion rate to the oscillations of the torus and related this to the boundary layer formed at the surface of the neutron star, finding that the most prominent mode of oscillation in the mass-accretion rate is the radial epicyclic mode, which they associated with the lower kHz QPO; they could not detect, however, the upper kHz QPO. We note therefore the analogy with our suggestion of searching an imprint of the torus’ oscillations on the mass-accretion rate, which is ultimately related to the boundary-layer luminosity, as demonstrated by Gilfanov et al. (2003) and Gilfanov & Revnivtsev (2005).

4 CONCLUSIONS

We have performed general-relativistic simulations of non-selfgravitating and axisymmetric tori with constant specific angular momentum orbiting around a nonrotating neutron star. After triggering oscillations via a small radial and vertical velocity perturbation, we have followed their evolution and setup a precise scheme

for the robust identification of the modes in the PSDs. In agreement with the linear analysis by Rezzolla et al. (2003b); Zanutti et al. (2003) and Zanutti et al. (2005), we have identified the fundamental p -mode frequency and its overtones, thus determining eight different frequencies of increasing value in the PSD of various hydrodynamical quantities, such as the rest-mass density. The peaks correspond to the modes of oscillation: f , o_1 , o_2 , $2f$, o_3 , $f + o_1$, $f + o_2$, and $3f$, as marked in the classification of Zanutti et al. (2005). Also in agreement with previous work on tori around black holes, we have found that the value of the fundamental frequency (and hence of the overtones) is inversely proportional to the torus size, scaling linearly with the mass of the star. The dependence of the frequencies on the size of the torus for a given neutron-star mass was then used to compare with the observational relation between the upper and the lower kHz QPOs in NS-LMXB 4U 1636–53. This was done by appropriately selecting pairs of peaks in the PSDs and relating each pair to the lower and upper kHz QPOs, ν_l, ν_u , with the goal of reproducing the observed linear relation.

Using the ten simulated models and taking into account all possible mode pairs, we have found that as long as we restrict our analysis to tori with constant specific-angular momentum, it is not possible to match the entire observational $\nu_l - \nu_u$ relation, although there are pairs of modes which either reproduce well the observed relation, e.g., modes o_2 and $f + o_1$, but in a limited frequency range, or have correct linear slope, e.g., modes o_1 and o_3 , but that require stellar masses $M \simeq 1.4 M_\odot$ and hence smaller than what expected from other analyses. Overall, while our simulations provide promising evidence that the phenomenology observed in 4U 1636–53 could be explained in terms of the p -mode oscillations of tori around the neutron star, it is also clear that the torus models considered here with a constant specific angular momentum can only provide a marginal match with the observed data. This is essentially due to the limitations set by the interplay between the torus size and the radius of the star.

These considerations promote at least three different directions in which our analysis can be improved and that we will consider in future work. First, we can extend this analysis to more general distributions of the specific angular momentum and determine whether the different tori sizes that will be allowed in this way will also provide a better match to the observations. Second, we can reconsider our models using fully three-dimensional simulations that would excite non-axisymmetric modes. It is then possible that, with a larger number of modes available, it will be easier to obtain a more accurate match with the observational data. Finally, we can deepen our astrophysical understanding of LMXBs by modelling the radiative processes thought to occur in these systems and their subsequent emission properties and signatures. In particular, using the results of the simulations coupled with the solution of the general-relativistic radiative transfer problem, we can produce synthetic spectra and light curves where time and phase lags will be an integral part of our modelling. In this way we will be able to study other properties of the QPOs, e.g., the fractional amplitude, and correlations with energy and frequency of the QPOs (see de Avellar et al. 2016).

ACKNOWLEDGEMENTS

MGBA acknowledges the financial support from FAPESP 2015/20553-0 and from the FAPESP Thematic Project 2013/26258-4. Additional support comes from “NewCompStar”, COST Action MP1304, the LOEWE-Program in HIC

⁴ In 4U 1636–53, the upper QPO varies from ~ 400 Hz at $HC = 1.0$ to ~ 1220 Hz at $HC = 0.65$; the lower QPO is detected at ~ 550 Hz for $(HC, SC) = (0.7, 0.98)$ and at ~ 890 Hz at $(HC, SC) = (0.62, 1.1)$.

for FAIR, the European Union’s Horizon 2020 Research and Innovation Programme (Grant 671698) (call FETHPC-1-2014, project ExaHyPE) and the ERC synergy grant "BlackHoleCam: Imaging the Event Horizon of Black Holes" (Grant No. 610058). MGBA is also grateful to the Institut für Theoretische Physik for the kind hospitality and to E. Ribeiro and P. Bult for the useful comments. ZY acknowledges support from an Alexander von Humboldt Fellowship.

REFERENCES

- Abramowicz M., Jaroszynski M., Sikora M., 1978, *Astron. Astrophys.*, **63**, 221
- Abramowicz M. A., Karas V., Kluźniak W., Lee W. H., Rebusco P., 2003, *Pub. Astron. Soc. Japan*, **55**, 467
- Abramowicz M. A., Kluźniak W., Stuchlik Z., Torok G., 2004, *ArXiv Astrophysics e-prints*,
- Altamirano D., van der Klis M., Méndez M., Jonker P. G., Klein-Wolt M., Lewin W. H. G., 2008, *Astrophys. J.*, **685**, 436
- Artigue R., Barret D., Lamb F. K., Lo K. H., Miller M. C., 2013, *Mon. Not. R. Astron. Soc.*, **433**, L64
- Bakala P., Goluchová K., Török G., Šrámková E., Abramowicz M. A., Vincent F. H., Mazur G. P., 2015, *Astron. Astrophys.*, **581**, A35
- Barret D., Olive J.-F., Miller M. C., 2006, *Mon. Not. R. Astron. Soc.*, **370**, 1140
- Blaes O. M., Arras P., Fragile P. C., 2006, *Mon. Not. R. Astron. Soc.*, **369**, 1235
- Blaes O. M., Šrámková E., Abramowicz M. A., Kluźniak W., Torkelson U., 2007, *Astrophys. J.*, **665**, 642
- Bursa M., Abramowicz M. A., Karas V., Kluźniak W., 2004, *Astrophys. J. Lett.*, **617**, L45
- Casares J., Cornelisse R., Steeghs D., Charles P. A., Hynes R. I., O’Brien K., Strohmayer T. E., 2006, *Mon. Not. R. Astron. Soc.*, **373**, 1235
- Daigne F., Font J. A., 2004, *Mon. Not. R. Astron. Soc.*, **349**, 841
- Di Salvo T., Méndez M., van der Klis M., 2003, *Astron. Astrophys.*, **406**, 177
- Done C., Gierliński M., Kubota A., 2007, *Astronomy and Astrophysics Reviews*, **15**, 1
- Douchin F., Haensel P., 2001, *Astron. Astrophys.*, **380**, 151
- Fishbone L. G., Moncrief V., 1976, *Astrophys. J.*, **207**, 962
- Font J. A., Daigne F., 2002, *Mon. Not. R. Astron. Soc.*, **334**, 383
- Gilfanov M., Revnivtsev M., 2005, *Astronomische Nachrichten*, **326**, 812
- Gilfanov M., Revnivtsev M., Molkov S., 2003, *Astron. Astrophys.*, **410**, 217
- Hasinger G., van der Klis M., 1989, *Astron. Astrophys.*, **225**, 79
- Kluźniak W., Abramowicz M. A., Kato S., Lee W. H., Stergioulas N., 2004, *Astrophys. J. Lett.*, **603**, L89
- Kozłowski M., Jaroszynski M., Abramowicz M. A., 1978, *Astron. and Astrophys.*, **63**, 209
- Lee W. H., Abramowicz M. A., Kluźniak W., 2004, *Astrophys. J. Lett.*, **603**, L93
- Lin Y.-F., Boutelier M., Barret D., Zhang S.-N., 2011, *Astrophys. J.*, **726**, 74
- Linares M., 2009, PhD thesis, Sterrenkundig Instituut “Anton Pannekoek - University of Amsterdam
- Liu B. F., Meyer F., Meyer-Hofmeister E., 2005, *Astron. Astrophys.*, **442**, 555
- Ludlam R. M., et al., 2017, *Astrophys. J.*, **836**, 140
- Lyu M., Méndez M., Altamirano D., 2014, *Mon. Not. R. Astron. Soc.*, **445**, 3659
- Mauche C. W., 2002, *Astrophys. J.*, **580**, 423
- Mazur G. P., Vincent F. H., Johansson M., Šrámková E., Török G., Bakala P., Abramowicz M. A., 2013, *Astron. Astrophys.*, **554**, A57
- Méndez M., 2006, *Mon. Not. R. Astron. Soc.*, **371**, 1925
- Miller M. C., Lamb F. K., Psaltis D., 1998, *Astrophys. J.*, **508**, 791
- Mishra B., Vincent F. H., Manousakis A., Fragile P. C., Paumard T., Kluźniak W., 2017, *Mon. Not. R. Astron. Soc.*, **467**, 4036
- Montero P. J., Zanotti O., 2012, *Mon. Not. R. Astron. Soc.*, **419**, 1507
- Montero P. J., Zanotti O., Font J. A., Rezzolla L., 2007, *Mon. Not. R. Astron. Soc.*, **378**, 1101
- Montero P. J., Font J. A., Shibata M., 2008, *Phys. Rev. D*, **78**, 064037
- Montero P. J., Font J. A., Shibata M., 2010, *Phys. Rev. Lett.*, **104**, 191101
- Novikov I. D., Thorne K. S., 1973, in *Black Holes (Les Astres Occlus)*. pp 343–450
- Parthasarathy V., Kluźniak W., Čemeljić M., 2017, *Mon. Not. R. Astron. Soc.*, **470**, L34
- Porth O., Olivares H., Mizuno Y., Younsi Z., Rezzolla L., Moscibrodzka M., Falcke H., Kramer M., 2017, *Computational Astrophysics and Cosmology*, **4**, 1
- Psaltis D., Belloni T., van der Klis M., 1999, *Astrophys. J.*, **520**, 262
- Reig P., van Straaten S., van der Klis M., 2004, *Astrophys. J.*, **602**, 918
- Remillard R. A., McClintock J. E., 2006, *Ann. Rev. Astron. Astroph.*, **44**, 49
- Rezzolla L., Zanotti O., 2013, *Relativistic Hydrodynamics*. Oxford University Press, Oxford, UK, doi:10.1093/acprof:oso/9780198528906.001.0001
- Rezzolla L., Yoshida S., Zanotti O., 2003a, *Mon. Not. R. Astron. Soc.*, **344**, 978
- Rezzolla L., Yoshida S., Maccarone T. J., Zanotti O., 2003b, *Mon. Not. R. Astron. Soc.*, **344**, L37
- Sanna A., Méndez M., Belloni T., Altamirano D., 2012, *Mon. Not. R. Astron. Soc.*, **424**, 2936
- Sanna A., Méndez M., Altamirano D., Belloni T., Hiemstra B., Linares M., 2014, *Mon. Not. R. Astron. Soc.*, **440**, 3275
- Schnittman J. D., Rezzolla L., 2006, *Astrophys. J.*, **637**, L113
- Shakura N. I., Sunyaev R. A., 1973, *Astron. Astrophys.*, **24**, 337
- Stella L., Vietri M., 1999, *Physical Review Letters*, **82**, 17
- Straub O., Šrámková E., 2009, *Classical and Quantum Gravity*, **26**, 055011
- Török G., Goluchová K., Horák J., Šrámková E., Urbanec M., Pecháček T., Bakala P., 2016, *Mon. Not. R. Astron. Soc.*, **457**, L19
- Vincent F. H., Mazur G. P., Straub O., Abramowicz M. A., Kluźniak W., Török G., Bakala P., 2014, *Astron. Astrophys.*, **563**, A109
- Warner B., Woudt P. A., 2002, *Mon. Not. R. Astron. Soc.*, **335**, 84
- Wijnands R., van der Klis M., 1999, *Astrophys. J.*, **514**, 939
- Wijnands R. A. D., van der Klis M., van Paradijs J., Lewin W. H. G., Lamb F. K., Vaughan B., Kuulkers E., 1997, *Astrophys. J. Lett.*, **479**, L141
- Zanotti O., Rezzolla L., Font J. A., 2003, *Mon. Not. R. Astron. Soc.*, **341**, 832
- Zanotti O., Font J. A., Rezzolla L., Montero P. J., 2005, *Mon. Not. R. Astron. Soc.*, **356**, 1371
- Zhang G., Méndez M., Sanna A., Ribeiro E. M., Gelfand J. D., 2017, *Mon. Not. R. Astron. Soc.*, **465**, 5003
- de Avellar M. G. B., Méndez M., Sanna A., Horvath J. E., 2013, *Mon. Not. R. Astron. Soc.*, **433**, 3453
- de Avellar M. G. B., Méndez M., Altamirano D., Sanna A., Zhang G., 2016, *Mon. Not. R. Astron. Soc.*, **461**, 79
- van Straaten S., van der Klis M., di Salvo T., Belloni T., 2002, *Astrophys. J.*, **568**, 912
- van Straaten S., van der Klis M., Méndez M., 2003, *Astrophys. J.*, **596**, 1155
- van Straaten S., van der Klis M., Wijnands R., 2005, *Astrophys. J.*, **619**, 455
- van der Klis M., 2006, *Rapid X-ray Variability*. pp 39–112

This paper has been typeset from a \LaTeX file prepared by the author.